Journal of
Advanced Manufacturing Science and Technology
jamst@jamstjournal.com；jamst2020@126.com
www.jamstjournal.com

Fracture prediction using damage models for incremental sheet forming process: A brief review

Kai ZHANG[a,*], Yuqing HU[a], Mingchuan WANG[b] , Zhenming YUE[c], Bing LIU[a], Chunjian SU[a,*]

[a] *College of Mechanical and Electronic Engineering, Shandong University of Science and Technology, Qingdao 266590, China*
[b] *Sino-French Engineer School, Nanjing University of Science and Technology, Nanjing 210094, China*
[c] *School of Mechanical and Electrical Engineering, Shandong University at Weihai, Weihai 264209, China*

Received 20 July 2024; revised 5 August 2024; accepted 27 August 2024; Available online 6 September 2024

Abstract: Incremental Sheet Forming (ISF) technology is a flexible and promising manufacturing technology to manufacture desired shape of sheet metals without using specific dies. The sheet subjected to incremental forming undergoes continuous deformation and frequently fails by fracture. In order to improve the formability, simulation of the ISF process until rupture of the sheet is essential. This paper provides a brief review on fracture prediction of incremental forming process based on uncoupled and coupled damage models, the predictive capability the of damage models in ISF process is compared via forming depth, final shape and crack paths. In addition, the theoretical aspects of various damage models are given in details, the merits and drawbacks of the damage models are carefully discussed. Finally, the paper offers insights into achieving high-quality, defect-free parts using incremental forming technology and highlights future trend in simulation of facture in ISF process.

Keywords: Incremental Forming; Fracture; Damage; Constitutive Model; Finite Element Simulation

1. Introduction

Due to the advent of a new industrial revolution, the manufacturing industry undergoes rapid changes in the global scale in past decades. Sheet metal forming technology plays an essential role in both customized mass and individualized production in the manufacturing industry [1, 2]. As shown in Fig. 1, flexibility and on-demand manufacturing has become important issues in recent sheet metal forming industry [3, 4]. For traditional sheet metal forming process, e. g. stamping, the shape of the part is dependent on the die, while Incremental Sheet Forming (ISF) could manufacture components with complex geometries without using specified die set [3], thus ISF process has high flexibility in forming sheet metals and has been widely employed in aerospace, architectural, prototyping, biomedical applications [4-6]. Various examples of practical application of ISF technology has been reported, Fig. 2(a) shows a self-bearing 3D roof structure consisting of 140 incrementally formed pyramids. Fig. 2(b) is a facade of tiger produced by ISF. Obviously, the ISF is very flexible forming technology in the current sheet metal forming industry [7, 8]. To date, various ISF processes have been developed, such as single point incremental forming (SPIF) [9, 10], two point incremental forming (TPIF) [11] with a positive or negative full die or a partial support, and double sided incremental forming (DSIF) [12]. Some additional energy fields has been used to enhance the formability of hard-to-deform materials, such as electropulsing assisted ISF and Electric hot ISF[13, 14].

In order to improve the forming quality, it is vital to understand the mechanisms that cause the plastic strain localization which eventually leads to ductile damage occurrence in the incremental forming process for sheet metal component [16, 17]. Damage is regarded as micro-defects density, which accumulates to a certain level before the initiation of macroscopic cracks [18, 19]. From the physical point of view, ductile damage is described as initiation, growth and coalescence of micro-cavities or micro-cracks induced by large plastic strains in the vicinity of inclusions in material [12, 20, 21]. In sheet metal applications, three failure phenomena are usually observed [22, 23]: (i) Ductile tensile fracture, (ii) ductile shear fracture and (iii) necking. Both diffuse necking and localized necking are two types of instability occurring before the sheet fracture. Diffuse necking is caused by a reduction of the waist over a length. Localized necking occurs inside the diffuse zone because of a reduction of thickness along a narrow band [24, 25]. Since the tool moves fast at the sheet surface and force the sheet to deform at the same time, the plastic deformation and damage mechanism are quite different from traditional forming process [13, 26, 27]. In order to avoid cracks and improve the forming quality of the component, efforts have been made at both experiments and simulations aspects [28, 29].

Finite Element (FE) simulation of the incremental forming pro-

* Corresponding author. *E-mail address:* kai.zhang@sdust.edu.cn (Prof. Kai ZHANG); suchunjian2008@163.com (Prof. Chunjian SU)
Peer review under responsibility of Editorial Committee of JAMST
DOI: 10.51393/j.jamst.2025011

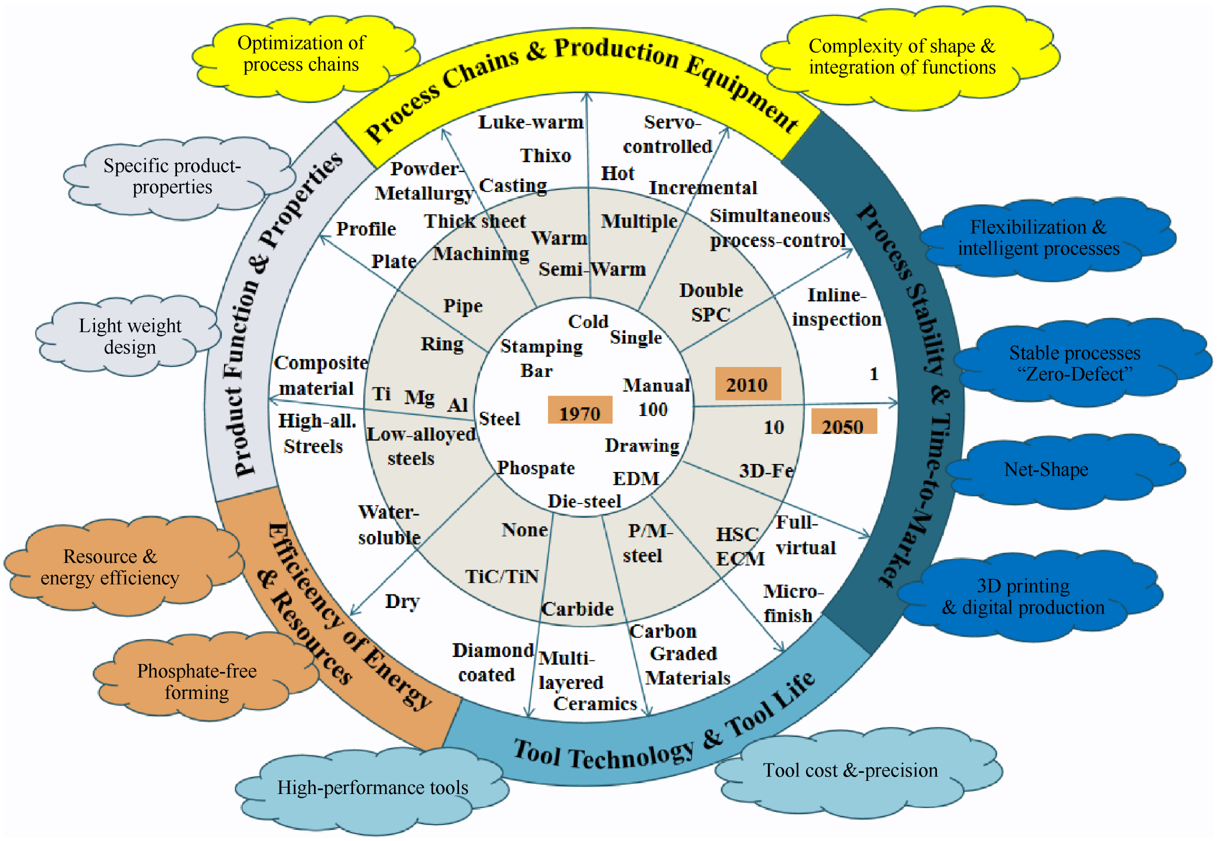

Fig. 1 Past and future of metal forming technology [15].

cess plays an important role in reveal the deformation mechanism and optimize the forming process [30], prediction of the ductile fracture behavior accurately and efficiently during incremental forming process is the key issue [31], which is relying on material constitutive models [32-34]. Since the computational cost is heavy for microscopic model, e.g. crystal plasticity model [35], it is not suitable for incremental forming process simulation. Thus, in this paper, we limited ourselves review for macroscopic models. In order to describe the ductile damage, many damage models at macroscopic scale can be found in literature [36]. They can be classified into three types [37]: (1) uncoupled damage models; (2) GTN damage models; (3) Continuum Damage Mechanics(CDM) models.

The uncoupled approaches are based on specific failure criteria written in terms of stress or strain invariants giving the final fracture when their critical values are reached [29, 38]. The advantage of these approaches are their simplicity by using the so-called failure indicators (criteria) which are easy to implement in FE software [39].

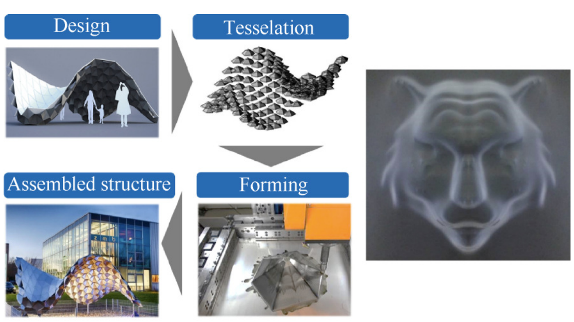

(a) (b)

Fig. 2 Self-bearing 3D roof structure developed at RWTH [11] and SPIF manufactured decorative element KULeuven [4].

Due to their uncoupled nature, the presence of micro-defects has no effect on mechanical fields (i.e. no interactions between the micro-defects and the material behavior or no coupling) [28]. So that these models do not consider stress and stiffness softening within the material caused by damage occurrence during deformation, which leads to an easy to use calibration of the material parameters.

For Gurson-type models, the influence of ductile damage in the yield condition is taken into account only on the yield function, by a porosity fraction and failure is predicted to occur when the porosity reaches a given critical value [40, 41]. The elastic stiffness is then not affected by damage (no decrease of the stiffness due to the damage occurrence). The first damage model within this approach was proposed by Gurson [40]. Later, Tvergaard and Needleman extended the Gurson model to include the void coalescence mechanism, this is called GTN model [41, 42].

The continuum damage mechanics (CDM) model is based on the thermodynamics framework leading to describe the ductile damage by a scalar or tensorial variable [43, 44]. Due to the strong coupling between the ductile damage and the material behavior, the material properties are deeply affected by the damage occurrence [45]. The concept of effective stress was first introduced by Kachanov to define the concept of continuum damage mechanics [44]. Since then, this kind of CDM approaches have been used for damage prediction in various situations assuming various types of coupling in many published works [46-49].

In this paper, the damage prediction of ISF process based on various constitutive models is reviewed. Section 2 illustrates the incremental forming systems, then the paper is structured according to the different types of damage models used for ISF process in Section 3 to 5. Finally, the review is concluded with some perspectives for simulation of the ISF process.

2. Incremental sheet forming systems

2.1 Existing types of incremental forming

Fig. 3(a) presents typical components in the basic setup of SPIF, namely, the blank holder plate, backing plate, and a ball end tool [50]. The backing plate rigidly holds the sheet in place, and a tool (typically mounted in a computer numerical controlled (CNC) machine) progressively deforms the sheet along a predefined path. Fig. 3(b) illustrates a double side incremental forming process [12], in comparison with SPIF, a slave tool is added in the opposite side to the master tool, which could have a better control of the sheet deformation.

Su et al. reported that the forming limit angle of the AZ31B magnesium alloy sheet increased as the forming temperature increased during SPIF process [31]. Since the temperature affect the formability of the sheet, Electric Hot Incremental Forming (EHIF) could offer localized heating of the sheet along the tool path, which could improve the formability of the sheet [14]. The schematic representation and Experimental equipment of EHIF is shown in Fig. 4. However, the EHIF has obvious shortcomings, because the tool is used to heat the sheet, when using small radius forming tool may lead to burning out the sheet, and there is no lubrication between the tool and sheet, which lead to damage of the surface of the sheet. To avoid these shortcoming without affect the heating effect, another method is heating the sheet by hot air blowers, based on this way a significant increase in formability could be achieved. Fig. 5 shows the schematic of the experimental equipment for electrically assisted SPIF for global heating of the AZ31 sheet [51].

2.2 Toolpath generation algorithms

Numerous research has been conducted to study the influence of parameters on the formability, geometric accuracy, and surface quality of ISF process. Notably, ISF process depends strongly on the forming tool path which influences greatly the part geometry and sheet thickness distribution. Contouring tool paths could be generated by CAM software [52-54]. The widely used toolpath layouts are z-level and zigzag-type toolpaths [4], as shown in Fig. 6. The vertical step size could affect the forming height of the ISF, which is dependent on the number to contours. Other parameters, e. g. tool diameter, blank thickness have also influence on the formability. To obtain defect-free work-piece with a short forming time, controlling the tool path during the forming process is vital. For example, to optimize the spiral tool path, the number of vertical pitches or tours is the most important targeted design parameter, Fig. 7 shows the different number of tours for a spirals tool path.

To achieve extreme formability during SPIF process, the simulation of the ISF process is essential. Fracture occurs quite often in the ISF process, among the review papers in literature, the amount of research focused on fracture prediction for ISF simulation is relatively few. Since damage prediction often needs more complex constitutive models, thus, in the next section, the fracture prediction for ISF process based on various damage models are summa-

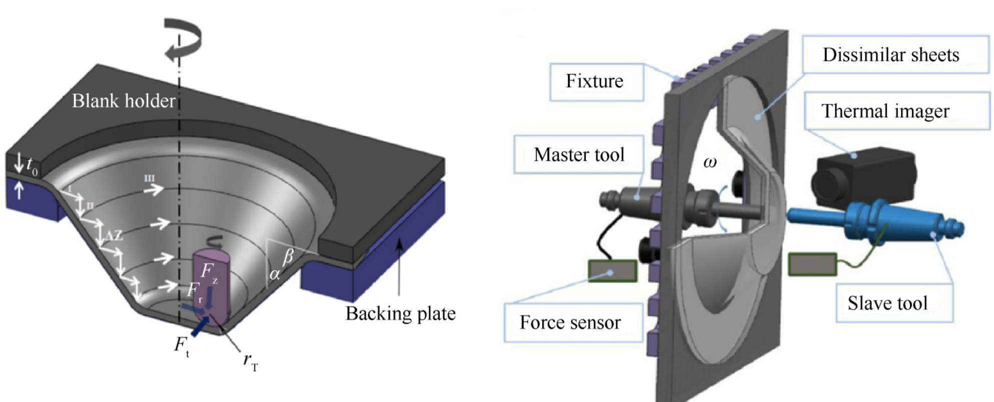

(a) (b)

Fig. 3 Schematic of incremental forming: (a) single point and (b) double side [12, 50].

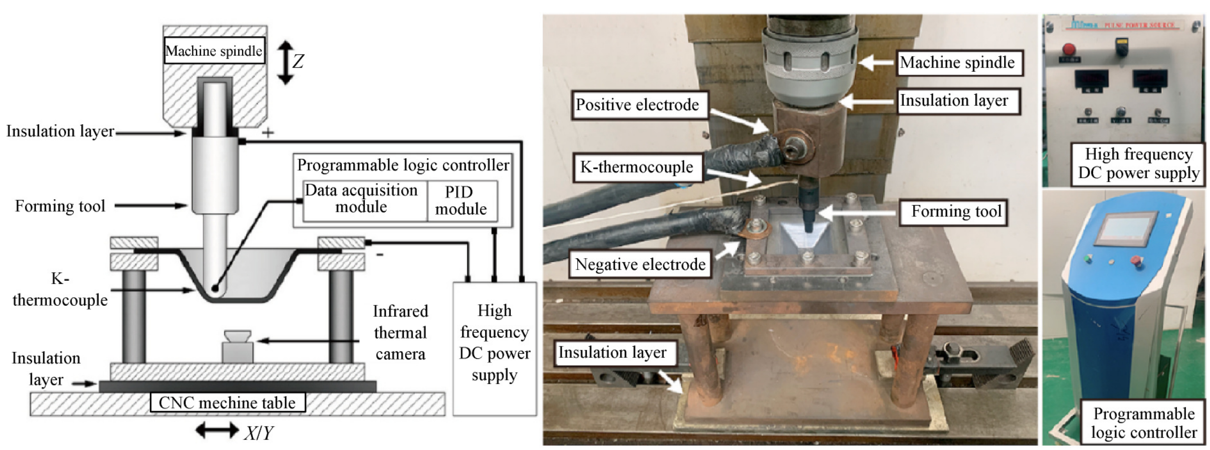

(a) (b)

Fig. 4 Experimental equipment of EHIF: (a) schematic structure, (b) actual setup [14].

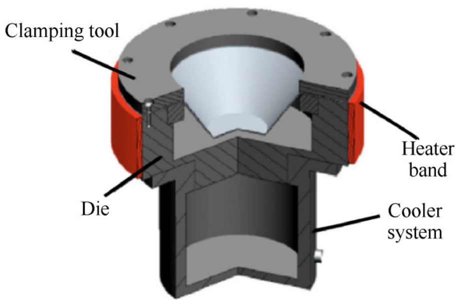

Fig. 5 Schematic of experimental equipment using global heating [51].

rized. To date, many damage models can be found in literature. In the paper, the fracture prediction based on three types of damage models, namely, (1) uncoupled damage model; (2) GTN damage models; (3) CDM damage model are presented in the following sections.

3. Uncoupled damage models

3.1 Theoretical aspects of uncoupled damage models

3.1.1 MMC model [56]

The evolution function of the Modified Mohr-Coulomb (MMC) model is expressed in integral formula as

$$D\left(\bar{\varepsilon}_{\mathrm{p}}\right)=\int_0^{\bar{\varepsilon}_{\mathrm{p}}}\frac{\mathrm{d}\bar{\varepsilon}_{\mathrm{p}}}{f\left(\eta,\bar{\theta}\right)} \tag{1}$$

where D is the damage accumulation value, it varys from $D\left(\bar{\varepsilon}_{\mathrm{p}}\right)=0$ to $D\left(\bar{\varepsilon}_{\mathrm{p}}\right)=1$ represent the undamaged and completely damaged state. The expression of $f\left(\eta,\bar{\theta}\right)$ is the same as Eq. (1), When the elastic strain is ignored, the equivalent plastic strain at the final fracture defines the fracture strain of the material, i. e., $\varepsilon_{\mathrm{f}}\approx\bar{\varepsilon}_{\mathrm{p}}$. the fracture strain is dependent on stress triaxiality normalized Lode angle as follows:

$$\varepsilon_{\mathrm{f}}=\left\{\begin{array}{l}\dfrac{A}{c_2}\left[c_3+\dfrac{\sqrt{3}}{2-\sqrt{3}}\left(1-c_3\right)\left(\sec\left(\dfrac{\pi\bar{\theta}}{6}\right)-1\right)\right]\times\\ \left[\sqrt{\dfrac{1+c_1^2}{3}}\cos\left(\dfrac{\pi\bar{\theta}}{6}\right)+c_1\left(\eta+\dfrac{1}{3}\sin\left(\dfrac{\pi\bar{\theta}}{6}\right)\right)\right]\end{array}\right\}^{-\frac{1}{n}} \tag{2}$$

where ε_{f} is facture strain, A and n are hardening parameters of Swift model, c_1, c_2, and c_3 are damage parameters of MMC model.

3.1.2 Wierzbicki damage model [38, 39, 57]

Wierzbicki damage model is a widely used uncoupled damage model because of its high efficiency in computation and simplicity in parameter identification. The equivalent plastic strain at the onset of fracture $\bar{\varepsilon}_{\mathrm{f}}$ is determined by the stress states. The state of damage initiation is defined by Eq. (3).

$$D_{\mathrm{c}}=\int_0^{\bar{\varepsilon}_{\mathrm{f}}}\frac{\mathrm{d}\bar{\varepsilon}_{\mathrm{p}}}{\bar{\varepsilon}_{\mathrm{f}}\left(\eta\right)} \tag{3}$$

For most metals the fracture strain is a dependent function of stress triaxiality η, as shown in Eq. (4).

$$\bar{\varepsilon}_{\mathrm{f}}\left(\eta\right)=\begin{cases}\infty & \left(\eta\leqslant-1/3\right)\\ C_1/\left(1+3\eta\right) & \left(-1/3\leqslant\eta\leqslant0\right)\\ C_1+\left(C_2-C_1\right)\left(\eta/\eta_0\right)^2 & \left(0\leqslant\eta\leqslant\eta_0\right)\\ C_2\eta_0/\eta & \left(\eta_0\leqslant\eta\right)\end{cases} \tag{4}$$

where η_0 is the mean value of stress triaxiality in uniaxial tension, C_1 and C_2 are $\bar{\varepsilon}_{\mathrm{f}}$ in pure shear and uniaxial stress state respectively. The Weirzbiki model has been extended to consider the effect of Lode angle to improve the predictive capability [39].

3.1.3 Hosford-Coulomb (HC) model [58]

Hosford-Coulomb (HC) fracture model assumes localization of deformation in a narrow zone and the localization criterion can be given as

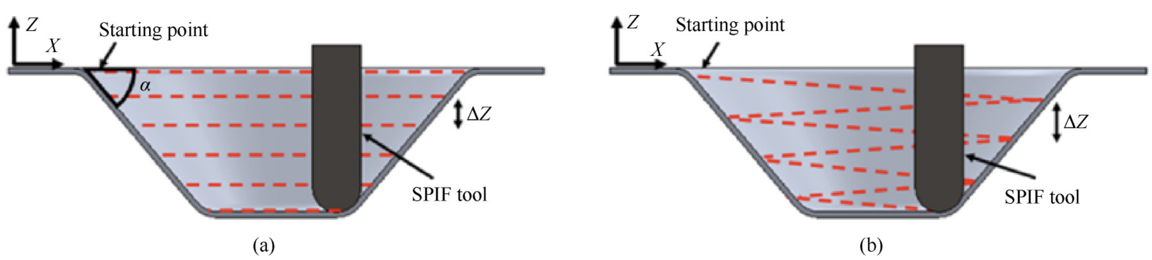

Fig. 6 Schematic of forming tool path: (a) Z-level tool path, (b) spiral tool path (zigzag-type) [4].

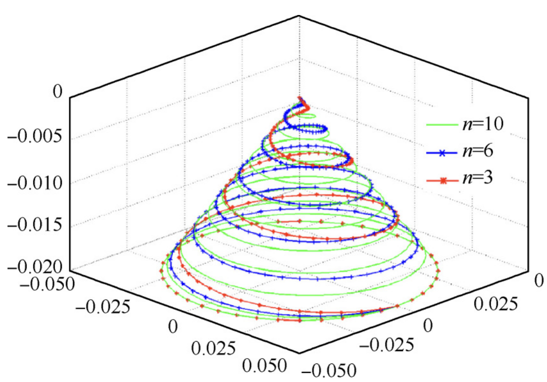

Fig. 7 Tool path with different number of tours [55].

$$\left\{\frac{1}{2}\left(\left(\sigma_1-\sigma_2\right)^a+\left(\sigma_2-\sigma_3\right)^a+\left(\sigma_3-\sigma_1\right)^a\right)\right\}^{1/a}+c\left(\sigma_1+\sigma_3\right)=b \tag{5}$$

where parameter a denote the Hosford exponent. c and b refer to cohesion and frictional terms respectively. The criterion in a stress-strain space $\left(\eta,\bar{\theta},\bar{\varepsilon}\right)$ by performing a transformation from the principal stress space $\left(\sigma_1,\sigma_2,\sigma_3\right)$, the Lode angle parameter dependent functions are as follows:

$$f_1\left[\bar{\theta}\right]=\frac{2}{3}\cos\left[\frac{\pi}{6}\left(1-\bar{\theta}\right)\right] \tag{6}$$

$$f_2\left[\bar{\theta}\right] = \frac{2}{3}\cos\left[\frac{\pi}{6}\left(3+\bar{\theta}\right)\right] \tag{7}$$

$$f_3\left[\bar{\theta}\right] = -\frac{2}{3}\cos\left[\frac{\pi}{6}\left(1+\bar{\theta}\right)\right] \tag{8}$$

The stress at the onset of fracture σ_f can be formulated as

$$\sigma_f\left(\eta,\bar{\theta}\right) = \frac{b}{\left\{\begin{array}{l}\left[\frac{1}{2}\left(\left(f_1-f_2\right)^a+\left(f_2-f_3\right)^a+\left(f_1-f_3\right)^a\right)\right]^{\frac{1}{2}} \\ +c\left(2\eta+f_1+f_3\right)\end{array}\right\}} \tag{9}$$

Based on the uncoupled damage models aforementioned, the fracture of ISF process is simulated by many researchers, the details are given in the following section.

3.2 Fracture prediction using uncoupled damage models

The numerical implementation of uncoupled damage models is relatively simple, and the identification of the material parameters is feasible with using several simple tests [59, 60]. Therefore, these model caught on in sheet metal forming industry. Mirnia et al. implemented the MMC ductile fracture criterion in prediction the onset of fracture of different shape of the cone [61]. Fig. 8 shows the experimentally observed fractured specimens and the predicted fracture in the FE simulation. From the comparison, the final crack path for all the parts depicted in Fig. 8 is located at the outside of the cone, the simulation results show good consistence with the experiments.

Ali Zahedi Dizajyekan predicted the ductile fracture and deformation behavior of the Al/Cu bimetallic sheets in the SPIF process using the Wierzbicki damage model [62]. The parameters of the damage model were calibrated separately for Al and Cu sheet, then using the model to obtain and the forming depth and the crack path of incremental forming of the bimetallic sheet. The damage distribution contours and the fracture depth at several frames after the onset of fracture for the bimetallic sheet in AC and CA layer arrangements are shown in Fig. 9, respectively. From the comparison of experimental and numerical results, it can be seen that the prediction accuracy of the damage model is satisfying, the predicted forming depth at fracture of various forming shape was with an average error of 5.38% and 7.27% for the AC and CA layer arrangements respectively.

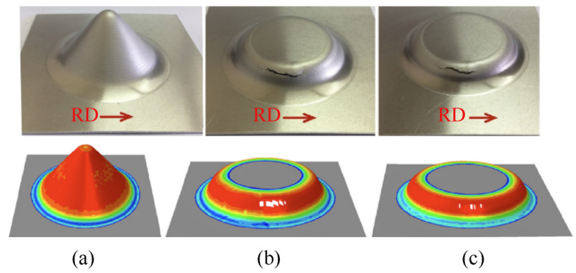

Fig. 8 Experimentally observed and predicted rupture using MMC model: the truncated cone with the wall angle of (a) 50°, (b) 60°, (c) 70° [61].

Bharti et al. conducted a comparative analysis of fracture prediction in incremental forming process with three uncoupled damage (HC, MMC and BW) models [63]. The material parameters of all the models were determined by the inverse method. For the hybrid five lobe forming case, the in-plane major and minor strain distribution at the end of forming simulation is compared to the experiments, as shown in Fig. 10. It can be observed that crack appears at the part walls of one lobe, and the crack path obtained by simulation using different damage models are reasonably identical to the experiments. By comparing with other forming test, it was observed that all the three models underestimate the fracture strain measured in ISF. The Hosford Coulomb (HC) damage model shows the best overall predictive capability among three damage models investigated for the given range of loading conditions, as shown in Table 1.

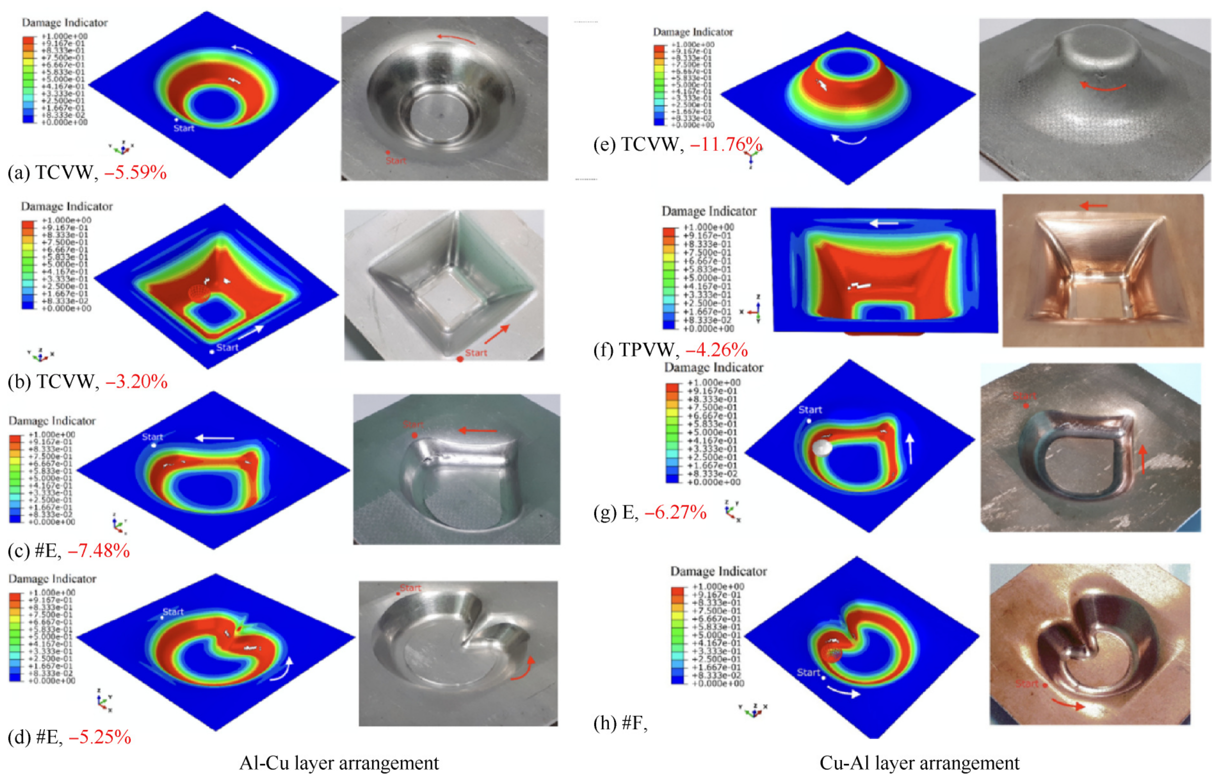

Fig. 9 The comparison of fracture in SPIF of Al/Cu two-layer sheets with different layer arrangement [62].

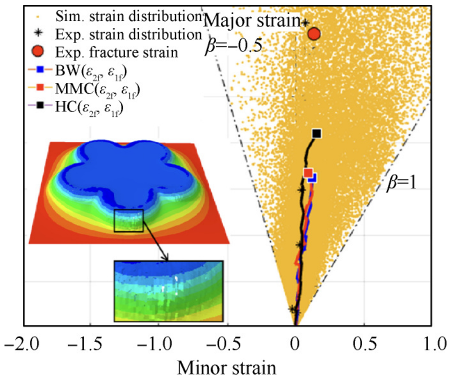

Fig. 10 In plane strain distribution for flower shape part [63].

Zhan et al. proposed a hybrid method by using analytical model and uncoupled ductile fracture criterion [64], in which the rise of temperature form friction heat is considered. The method is applied to predict the failure distribution on the thickness, to reveal the damage mechanism along thickness direction. Fig. 11 shows experimental and simulation results for a hybrid shape (HS) with concave and convex curvatures. As shown in Fig. 11, the predicted forming depth is 11.19 mm which is slightly underestimated to the experimental forming depth is 13.10 mm. The fracture and micro-crack appears on the outer surface, the predicted crack path is in good agreement with experiment.

4. GTN damage model

4.1 Theoretical aspects of GTN model

The GTN model was developed based on a continuous damage model for isotropic materials proposed by Gurson [40], the original model considers hydrostatic stress to capture the void growth in damage accumulation. Based on the consideration of the voids behavior, this model was extended by introducing an equivalent void volume fraction [41] into the yield function to enhance the description material degeneration a realistic void volume fraction. The classical GTN damage model is expressed by Gurson potential Φ as shown in Eq. (10):

$$\Phi = \left(\frac{\Sigma_{eq}}{\sigma_F}\right)^2 + 2q_1 f^* \cosh\left(\frac{3q_2\sigma_H}{2\sigma_F}\right) - 1 - \left(q_1 f^*\right)^2 = 0 \quad (10)$$

where Σ_{eq} is equivalent stress, σ_F is an effective stress measure depending on both the stress tensor and the void volume fraction, σ_H is the trace of Cauchy stress. q_1 and q_2 are two parameters, since they have no physical meaning, it is not easy to calibrated their values, they usually take the suggested values based on numerical investigation from literature, for example, Tvergaard and Needleman [41] recommended to set the value of these parameter: q_1= 1.5, q_2= 1. Parameter f^* describe the porosity evolution and coalescence in segment function form:

$$f^* = \begin{cases} f, f < f_c \\ f_c + \left(f - f_c\right)/\left(q_1 - f_c\right)\left(f_f - f_c\right), f \geqslant f_c \end{cases} \quad (11)$$

where f_c is the critical porosity and f_f is the failure porosity. The effective porosity f is consisted of void growth and nucleation. The evolution law of nucleation and growth of voids primarily cause the variation of void volume fraction, as follows:

$$\dot{f} = \dot{f}_{growth} + \dot{f}_{nucleation} \quad (12)$$

$$\dot{f}_{growth} = \left(1 - f\right)\dot{e}^p_{kk} \quad (13)$$

$$\dot{f}_{nuleation} = \frac{f_n}{s_N\sqrt{2\pi}}\exp\left[-\frac{1}{2}\left(\frac{e_p - e_n}{s_N}\right)^2\right] \quad (14)$$

where $\dot{f}_{nucleation}$ and $\dot{f}_{growth}$ represent the damage rate related to damage nucleation and void growth, the e^p_{kk} is the trace of the plastic strain rate tensor, f_n is the total potential void volume fraction for nucleation; e_n and s_N are the average value and standard deviation in the normal distribution of the nucleation strain; e_p is the equivalent plastic strain. To capture the damage under shear dominant path, various extensions were proposed by embedding the Lode angle parameter [65, 66]. The variation of void volume fraction caused by shear in damage contribution $\dot{f}_{shear}$ is added in the evolution function as follows:

$$\dot{f} = \dot{f}_{growth} + \dot{f}_{nucleation} + \dot{f}_{shear} \quad (15)$$

$$\dot{f}_{shear} = k_w \omega(\sigma) f \frac{\sigma:\dot{\varepsilon}^p}{\bar{\sigma}} \quad (16)$$

$$\omega(\sigma) = 1 - \left(\frac{27J_3}{2\bar{\sigma}^3}\right)^2 \quad (17)$$

where k_w is the parameter influence the shear stress during the deformation, which can be evaluated by calibration experiments. $\dot{\varepsilon}^p$ is the plastic strain rate, $\bar{\sigma}$ is effective stress, J_3 is third invariant of stress. ω is defined by the stress invariant, lies in the range from zero to one. The shear induced damage will be neglected with ω = 0

Table 1 Predicted and experimentally observed forming height at fracture in different ISF processes [63].

ISF	(LT)	Pyramid	(VWACF)	(5 Lobe)
BW damage criteria				
Exp.(mm)	12	16.82	40	12
FEM(mm)	10.57	9.01	28.52	8.27
Error(%)	11	46	28	31
MMC damage criteria				
Exp.(mm)	12	16.82	40	12
FEM(mm)	11.75	9.47	29.90	8.74
Error(%)	2	43	25	27
HC damage criteria				
Exp.(mm)	12	16.82	40	12
FEM(mm)	11.9	9.47	39.78	9.91
Error(%)	0.8	43.6	0.5	17.4

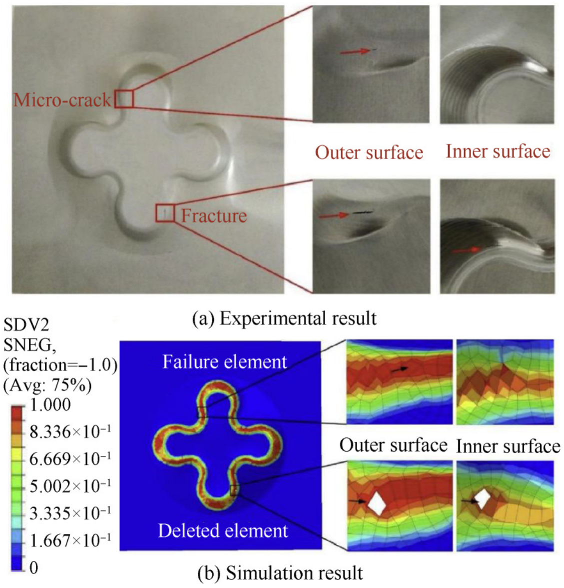

Fig. 11 Comparison of experimental and simulation results for ISF of hybrid shape [64].

under axisymmetric stress state, when $\omega = 1$ the maximum shearing effect for plane strain state is reached.

4.2 Fracture prediction using GTN model

Since the loading path during the ISF process is complex, using classic GTN model seems not adequate for accurate prediction. It is important to reveal the shear effect to the formability in ISF processes. Gatea et al. applied a modified GTN damage model to predict ductile fracture in the incremental forming process due to void nucleation and coalescence [67]. Fig. 12 shows the predicted void volume fraction values of both original and shear enhanced GTN models. It is found that shear could accelerate the fracture and it is near to the experimental fracture depth. Obviously, shear has evident effect in the stretching along the meridional direction to develop the fracture in incremental forming process. As shown in Fig. 13, the crack appears at the corner of truncated pyramid with a depth of 28.64 mm and 25.5 mm predicted by the original and shear enhanced GTN models respectively, and the simulation results by modified model shows that it is closer to the experimental measured depth of 26.7 mm. Thus, the FE result of the shear enhanced GTN model was in a good agreement with experiments. The final crack path appears at the corner area due to biaxial stretching deformation mode as compared to a plane strain stretching along the straight side.

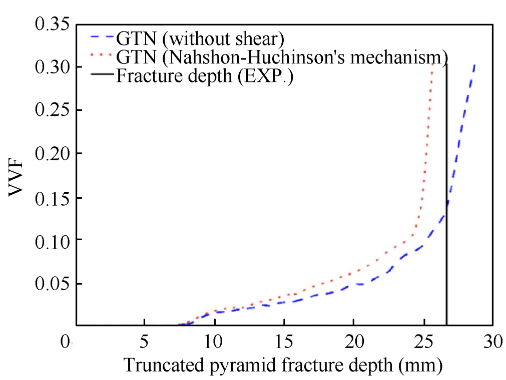

Fig. 12 Comparison between GTN models with and without shear of truncated pyramid [67].

Chang et al. observed that the mechanism of void development in ISF process has its own character [68]. As shown in Fig. 14 the growth of void clusters along thickness direction is restrained, these void clusters could not become cracks. In addition, the dimension of void is prone to increase along meridional direction, which leads to the continuous increasing of the critical void size inside the sheet metal without rupture. Thus, the void volume fraction during ISF is much higher than that in uniaxial tension. This is considered to be the principal cause for the improved plasticity of ISF.

Considering the deformation mechanism during ISF process, the parameter represents the void cluster and orientation angle are taken into account to describe the shape of void cluster [68]. The simulation results of incremental forming processes for conical sample and pyramid sample of two aluminum alloys AA2024 and AA6061 are given in Fig. 15, the fractures located at the outside of wall, from the comparison, it is concluded that the force-displacement curves predicted by the proposed model are in good accordance with the experimental result, which demonstrate the predictive capability of the new model.

Peng and Ou proposed a new GTN model with considering the stress state effect, the model was applied to simulate the SPIF and DSIF process [69]. As shown in Fig. 16, it was found that the predicted crack path and forming height at fracture are in good agreement with the experiments. While the original model underestimates the forming depth with large error. It should be mentioned that the paper gives comprehensive analysis on stress state evolution during different deformation stages and the concomitant damage evolutions, as shown in Fig. 17, which demonstrates clearly that the strain path of ISF process undergoes with high complexity.

5. Continuum Damage Mechanics model

5.1 Theoretical aspects of CDM model

In the framework of continuum damage mechanics, ductile damage occurrence results from a progressive deterioration process of each material point including nucleation, growth and coalescence of microvoids and microcracks. The continuum mechanics approach can be applied to provide the constitutive and evolution equations under the framework of the thermodynamics of irreversible processes with state variables [70,71]. The model includes combined isotropic and kinematic hardening with isotropic ductile damage [72,73]. The specific Helmholtz free energy Ψ is defined in the fictive undamaged configuration, Ψ^e and Ψ^p are the elastic and plastic parts of the state potential Ψ.

$$\begin{aligned}\rho\Psi\left(\underline{\varepsilon}^{e},\underline{\alpha},r,d\right) &= \rho\Psi\left(\underline{\tilde{\varepsilon}}^{e},\underline{\tilde{\alpha}},\tilde{r}\right)\\ &= \rho\Psi^{e}\left(\underline{\tilde{\varepsilon}}^{e}\right)+\rho\Psi^{p}\left(\underline{\tilde{\alpha}},\tilde{r}\right)\end{aligned} \tag{18}$$

$$\begin{aligned}\rho\Psi^{e}\left(\underline{\tilde{\varepsilon}}^{e}\right) = \rho\Psi^{e}\left(\underline{\varepsilon}^{e},d\right) &= \frac{1}{2}\underline{\tilde{\varepsilon}}^{e}:\underline{\underline{\Lambda}}:\underline{\tilde{\varepsilon}}^{e}\\ &= \frac{1}{2}\left(1-d\right)\underline{\varepsilon}^{e}:\underline{\underline{\Lambda}}:\underline{\varepsilon}^{e}\end{aligned} \tag{19}$$

$$\begin{aligned}\rho\Psi^{p}\left(\underline{\tilde{\alpha}},\tilde{r}\right) = \rho\Psi^{p}\left(\underline{\alpha},r,d\right) &= \frac{1}{3}C\,\underline{\tilde{\alpha}}:\underline{\tilde{\alpha}}+\frac{1}{2}Q\tilde{r}^{2}\\ &= \frac{1}{3}\left(1-d\right)C\,\underline{\alpha}:\underline{\alpha}+\frac{1}{2}\left(1-d^{\gamma}\right)Qr^{2}\end{aligned} \tag{20}$$

where ρ is the mass density, $\underline{\underline{\Lambda}} = 2\mu_e\underline{1} + \lambda_e\underline{1}\otimes\underline{1}$ is the elastic fourth-rank operator defined by Lame's constant μ_e and λ_e. Parameters C and Q are the kinematic and isotropic hardening moduli of undamaged material.

By considering the rate independent plasticity dissipation, the generalized standard material framework is used assuming the non-

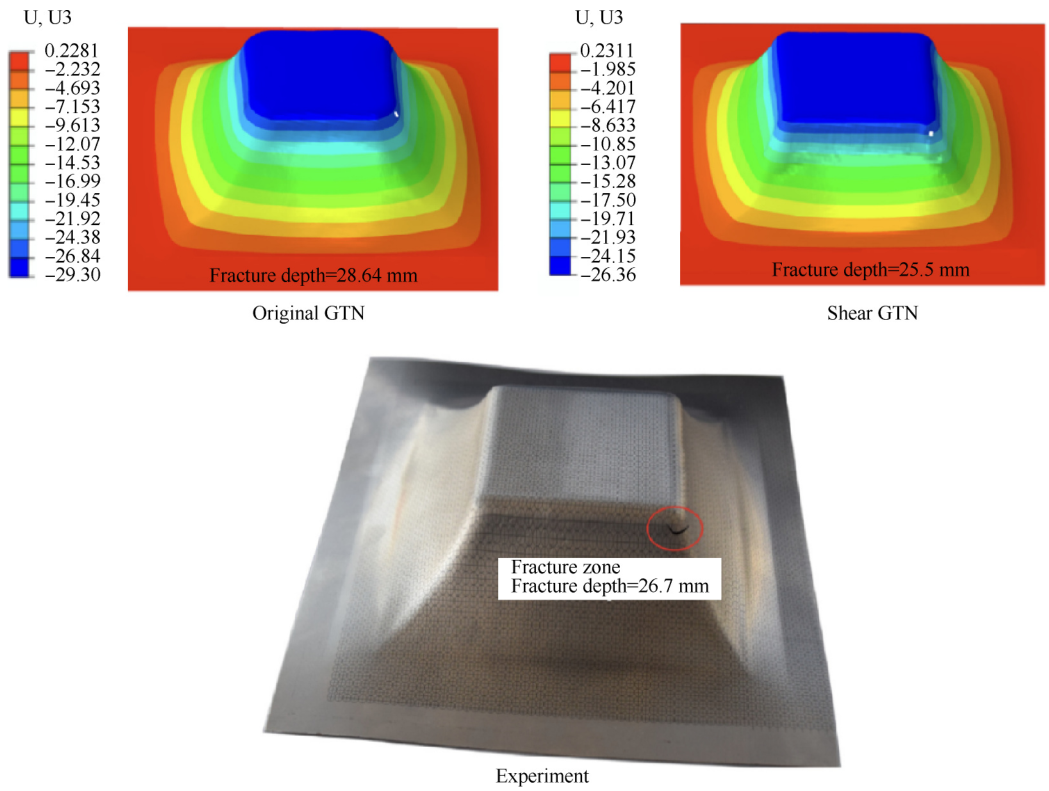

Fig. 13 Simulated results from original and shear modified GTN model in comparison with actual experiment of truncated pyramid [67].

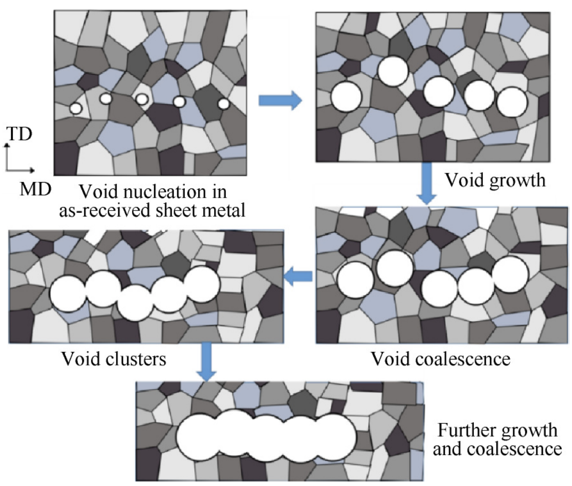

Fig. 14 Evolution mechanism of void in ISF [68].

associative plasticity theory in order to define the flux variables ($\underline{D}^p$, $\underline{\alpha}$, $\dot{r}$, $\dot{d}$). For this single surface theory, this leads to introduce a yield function $f(\underline{\sigma}, \underline{X}, R, d)$ and a plastic potential $F(\underline{\sigma}, \underline{X}, R, Y, d)$, both positive and convex functions of their main arguments are in the effective stress space.

$$f = \frac{\|\underline{S} - \underline{X}\|_H}{\sqrt{1-d}} - \frac{R}{\sqrt{1-d^\gamma}} - \sigma_y \quad (21)$$

$$F = F_p + F_d \quad (22)$$

$$F_p = f + \frac{3a(\underline{X}:\underline{X})}{4C(1-d)} + \frac{bR^2}{2Q(1-d^\gamma)} \quad (23)$$

$$F_d = \frac{S}{(s+1)(1-d)^\beta}\left\langle \left. \frac{Y - Y_0}{S} \right| \right\rangle \quad (24)$$

where $\|\underline{S} - \underline{X}\|$ is the equivalent stress which can be taken as isotropic and anisotropic equivalent stress.

Using the state potential in Eq. (18), the stress variables are determined as follows:

Cauchy stress tensor:

$$\underline{\sigma} = \rho \frac{\partial \Psi}{\partial \underline{\varepsilon}^e} = 2\mu_e(1-d)\underline{\varepsilon}^e + \lambda_e(1-d)tr(\underline{\varepsilon}^e)\underline{1} \quad (25)$$

Kinematic hardening:

$$\underline{X} = \rho \frac{\partial \Psi}{\partial \underline{\alpha}} = \frac{2}{3}(1-d)C\underline{\alpha} \quad (26)$$

Isotropic hardening:

$$R = \rho \frac{\partial \Psi}{\partial r} = (1-d^\gamma)Qr \quad (27)$$

Damage force:

$$Y = -\rho \frac{\partial \Psi}{\partial d} = Y^e + Y^\alpha + Y^r \quad (28)$$

From the plastic potential in Eq. (23), the evolution equations for the strain-like variables are given as follows:

Plastic strain tensor:

$$\underline{D}^p = \dot{\lambda}\frac{\partial F}{\partial \underline{\sigma}} = \frac{\dot{\lambda}}{\sqrt{1-d}}\underline{\tilde{n}} \text{ with } \underline{\tilde{n}} = \frac{\underline{\underline{H}}:(\underline{S} - \underline{X})}{\|\underline{S} - \underline{X}\|} \quad (29)$$

Kinematic hardening strain:

$$\underline{\alpha} = -\dot{\lambda}\frac{\partial F}{\partial \underline{X}} = \dot{\lambda}\left(\frac{1}{\sqrt{1-d}}\underline{\tilde{n}} - a\underline{\alpha}\right) \quad (30)$$

Isotropic hardening strain:

$$\dot{r} = -\dot{\lambda}\frac{\partial F}{\partial R} = \dot{\lambda}\left(\frac{1}{\sqrt{1-d^\gamma}} - br\right) \quad (31)$$

Isotropic damage rate:

$$\dot{d} = \dot{\lambda}\frac{\partial F}{\partial Y} = \frac{\dot{\lambda}}{(1-d)^\beta}\left(\langle Y - Y_0 | S \rangle\right) \quad (32)$$

where a and b are material coefficients defining the nonlinear evolution of kinematic and isotropic hardening, S, s, Y_0, β and γ are damage parameters [23].

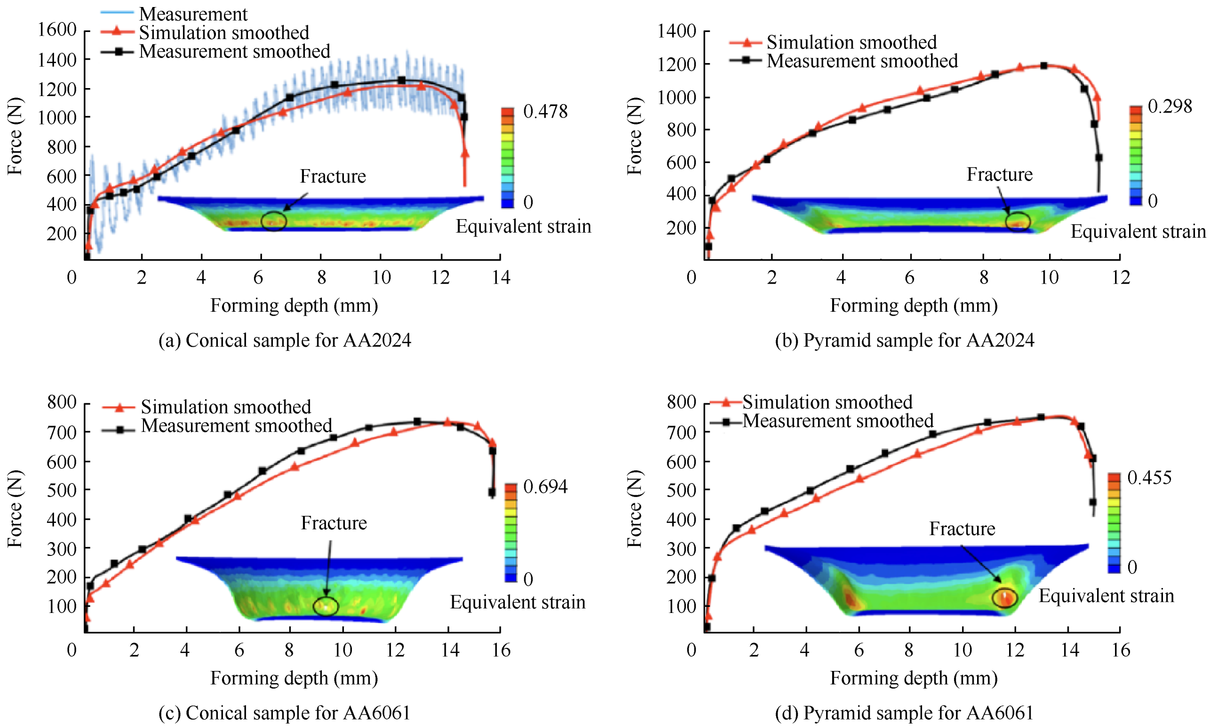

Fig. 15 Comparison of experimental and predicted force-displacement curves [68].

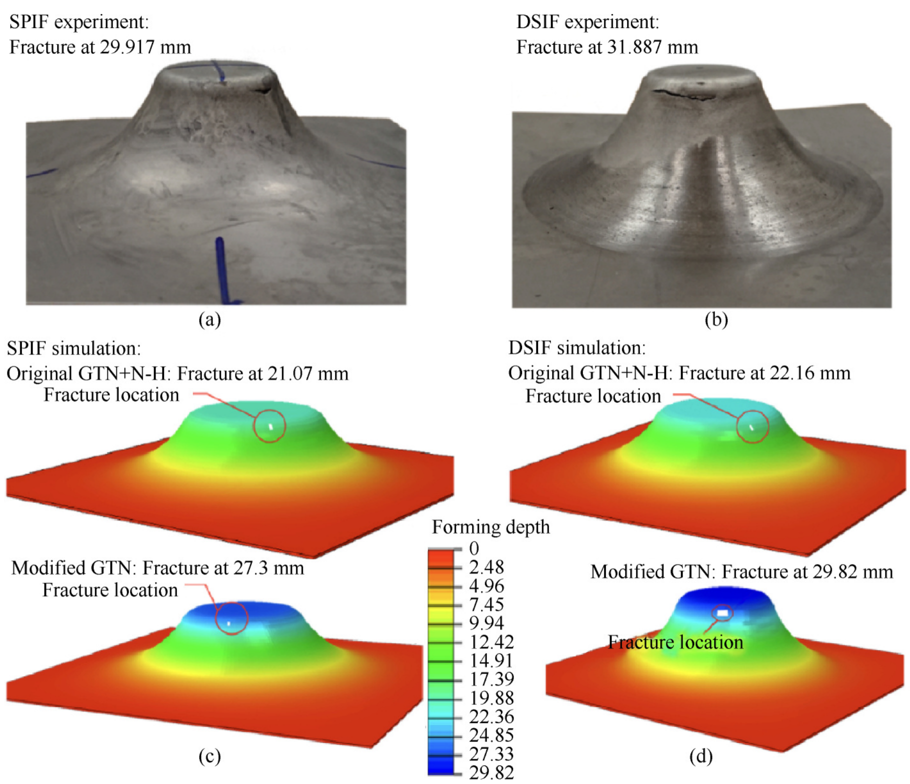

Fig. 16 Comparison of simulation results with experiment of SPIF and DSIF process [69].

5.2 Numerical simulation based on CDM model

Ben Said et al. simulated the plastic and damage evolution in single point incremental forming process using CDM model with Hill48 yield criterion and mixed non-linear isotropic/kinematic hardening [74]. The experimental results including thinning along rolling direction and thickness in function of the depth of the manufactured part (see Fig. 18) are used to validate the prediction capability of the CDM model. The predicted results of AA1050 was compared to truncated cone SPIF experiments which shows tiny distinction between the predicted and experimental thinning results. Therefore, it is noted that the CDM model could simulate the single point incremental forming process with good accuracy and efficiency. Bouhamed et al. proposed a non-associated ductile damage model under the CDM approach, the model could predict the formability of anisotropic sheet metals under incremental forming process with good accuracy. Numerical prediction of stress triaxiality distributions (see Fig. 19) during SPIF demonstrate that the stress states vary distinctively during the forming path [75].

The CDM damage models combined with nonlinear kinematic hardening and isotropic hardening has been applied to the predict the necking during incremental forming process [76]. The thickness and outer radius with respect to the forming depth of the sheet has been accurately predicted by the model, as shown in Fig. 20, meanwhile, the local necking occurs when the forming depth reaches16.5 mm, the numerical results show good agreement with the experiments. It can be found the damage model based on CDM approach can predict precisely the deformation and necking behavior during ISF process.

Yue et al. performed the SPIF simulation using CDM model considering yield surface distortion [77]. The equivalent plastic strain and ductile damage contours with and without distortion effect were compared when the drawing depth was 10 mm, as shown in Fig. 21, the numerical predicted equivalent plastic strain and ductile damage had different values. When considering the yield surface distortion, the sheet prone to be completely damaged (d = 1.0 denotes the full damage) at the outside of the wall. While the maximum value of damage d is 0.057 without yield surface distortion,

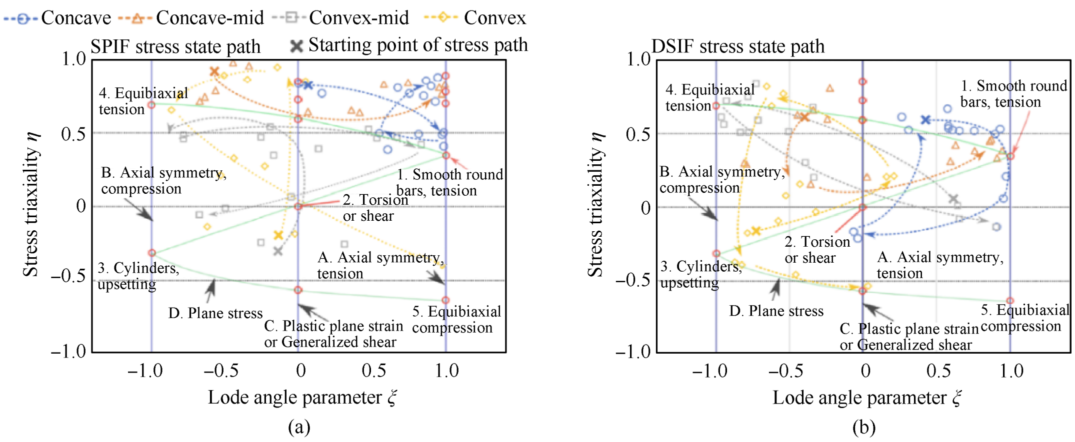

Fig. 17 Evolution of stress triaxiality and Lode angle parameter in (a) SPIF; (b) DSIF [69].

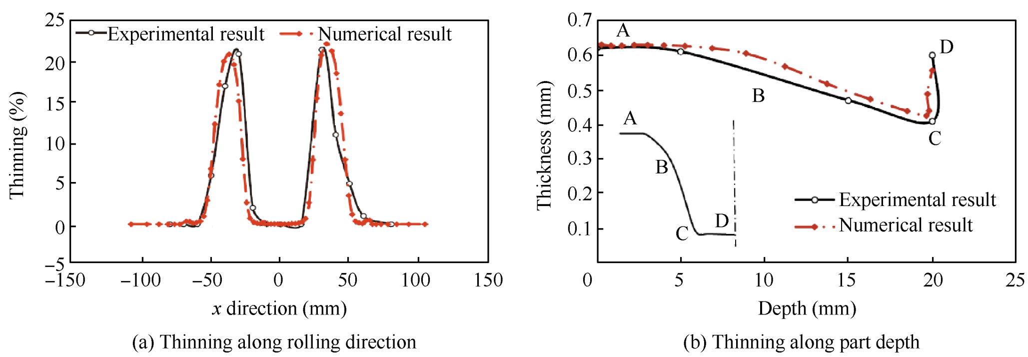

Fig. 18 Thinning comparison of simulation and experiments [74].

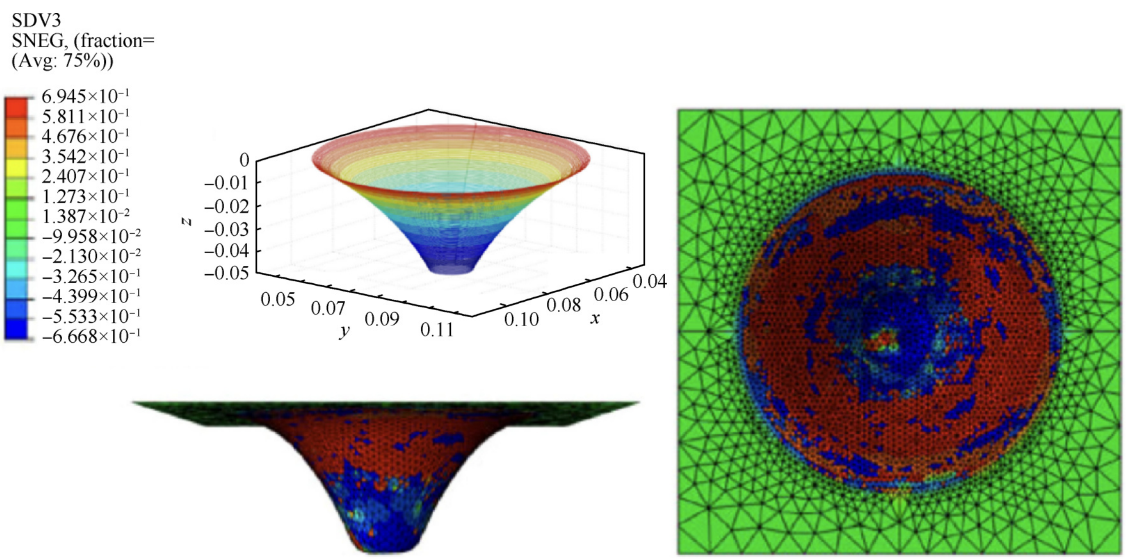

Fig. 19 Stress triaxiality distribution during the SPIF process [75].

which demonstrates that the yield surface distortion has obvious influence on the ISF process.

An enhanced Continuum Damage Mechanics (CDM) model was applied for ductile damage prediction in SPIF process [78]. In particular, the stress state dependence was considered in the damage evolution to improve fracture prediction capability at various loading paths. The enhanced CDM model was implemented into finite element code ABAQUS/Explicit through user subroutine VUMAT. The accuracy of the finite element model to predict the failure during SPIF process was investigated, good agreements were found between the simulation results and the experimental observations. Fig. 22 compares the predicted crack path and the fracture depth of the SPIF with the experiments. It is shown that the predicted crack path was in consistent with the actual experiments [67]. In addition, the predicted forming depth (31.7 mm) at fracture was in good agreement with the experimental result (31.1 mm) reported by

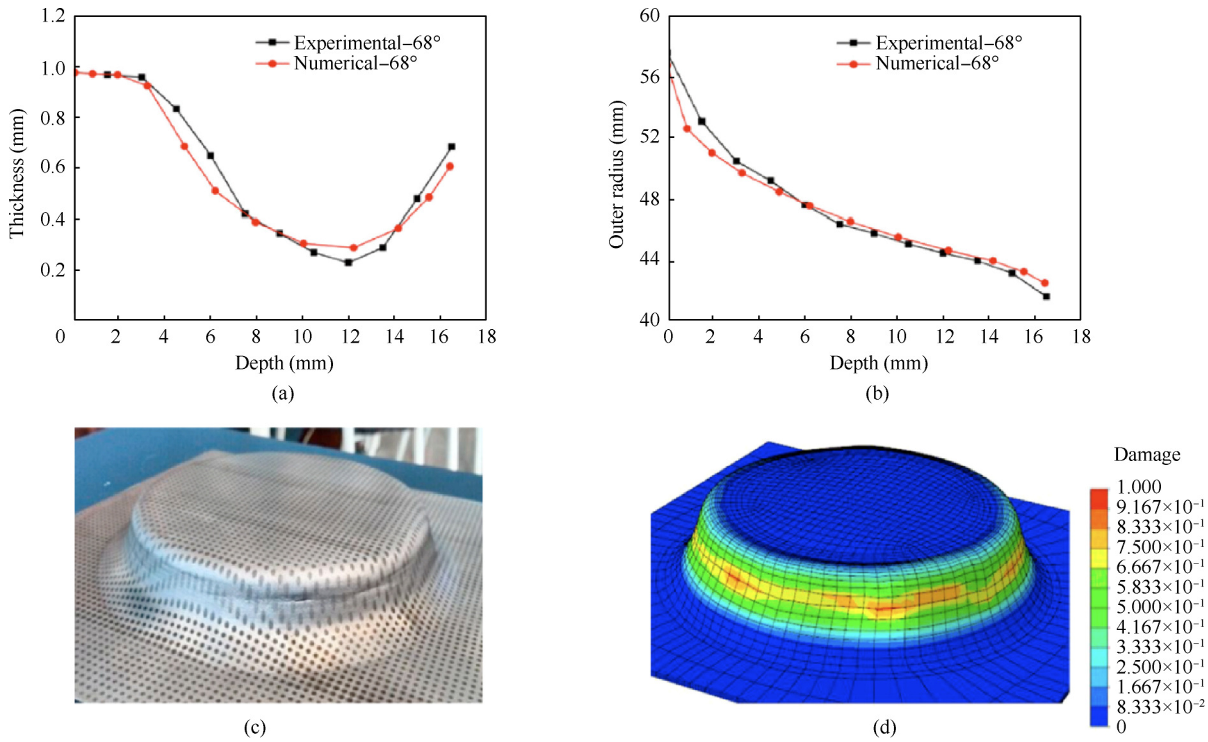

Fig. 20 Comparison of experiment and simulation results:(a)thickness, (b)outside diameter profile, (c)experiments, (d) predicted necking distribution [76].

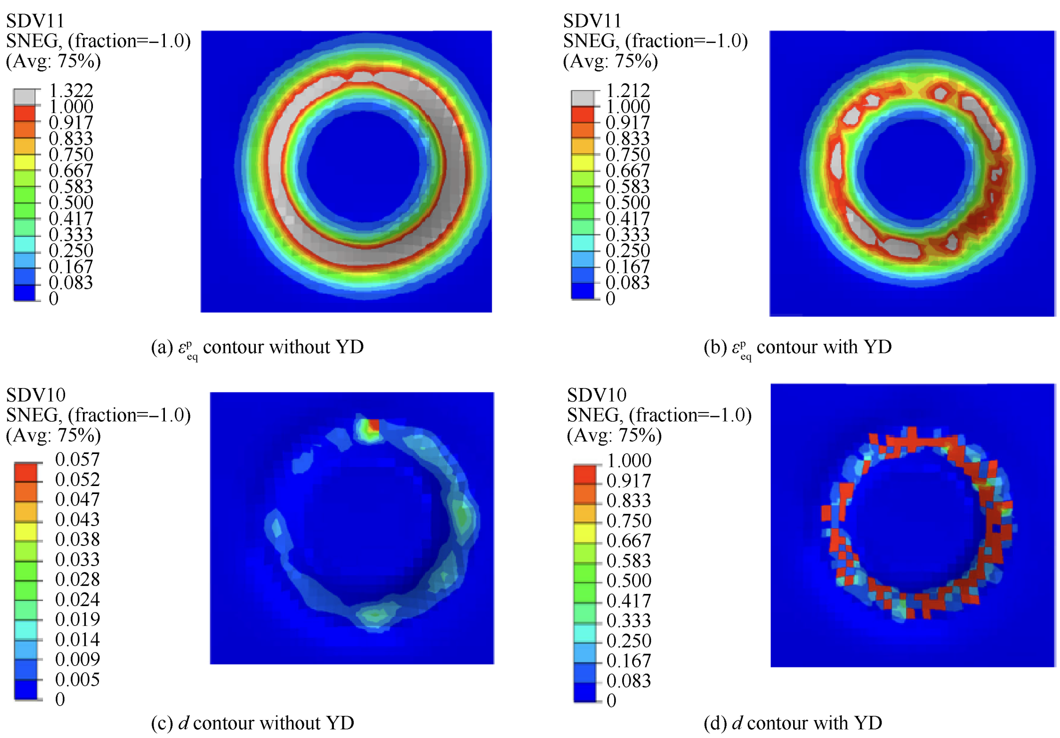

Fig. 21 Comparison of predicted equivalent plastic strain (SDV11) and ductile damage with and without yield surface distortion [77].

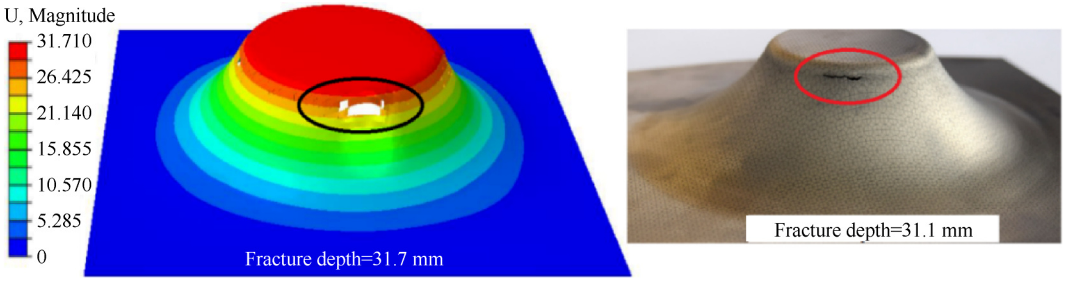

Fig. 22 Predicted crack path using the enhanced CDM model in comparison with experiment of the hyperbolic truncated cone SPIF process [78].

Gatea et al [67]. From all the comparison of simulation results and experiments, the enhanced CDM damage model could correctly predict the damage evolution and fracture during ISF process.

6. Conclusions

A review of fracture prediction of incremental forming process for manufacturing complex-shaped components was conducted. The paper has discussed research studies for various damage models and addressing their advantages and limitations, simulations based on these models were carefully analyzed and compared with experiments of ISF processes, the main conclusions can be summarized as follows:

(1) All the three macroscopic damage models have high computational efficiency in simulation of ISF process. The uncoupled damage models are easy to implement in the simulation, since their simple function form and identification procedure. The crack path could be predicted by the uncoupled damage models with stratifying accuracy. However, as the uncoupled nature, the accuracy of these models still need to be improved for ISF process since the forming path is very complex.

(2) The GTN damage model considers the void nucleation, growth and coalescence during large plastic deformation, while the fracture prediction using original GTN model shows obvious distinction with the experimental, which illustrates that the void evolution mechanism of ISF process is not the same with traditional forming process. Therefore, the deformation mechanism of ISF process was taken into account to enhance the description of the void evolution for GTN models, the simulation results from modified GTN models shows good agreement with the experiments. However, the shortcoming of using GTN models rely on the identification of the material parameters, since some parameters have no physical meaning.

(3) Fracture prediction using CDM approach is relatively less than GTN and uncoupled damage models, the CDM model is convenient in coupling various physical phenomena and shows satisfying simulation accuracy during ISF process. However, the damage at the surface during ISF process could not be well captured, thus the damage accumulation law under complex loading path should be further improved to adapt for complex ISF simulation.

(4) It is found that Artificial Intelligence (AI)-based computational methods e.g. artificial neural networks, deep learning technique, shows great potential in solving sheet metal forming relevant problems [79]. These models are faster than traditional modelling techniques and provide satisfying results [80]. However, it should be recognized that the predictive capability of the AI-based computational models are highly dependent on the amount of data which usually obtained from experiments. Thus, using solely the AI-based models in ISF simulation is not an economic way. To the authors' knowledge, the combination of physical constitutive models and AI-based computational models seems promising in future simulation of ISF process.

Acknowledgments

The financial support by the National Natural Science Foundation of China (No. 52205392) and Shandong Provincial Natural Science Foundation (No. ZR2022ME032) is acknowledged. The support by the Project of Shandong Province Higher Educational Young Innovative Talent Introduction and Cultivation Team (Intelligent Transportation Team of Offshore Products) is also appreciated.

References

1. Bai D, Gao P, Yan X, et al. Intelligent forming technology: State-of-the-art review and perspectives. *J Adv Manuf Sci Tech* 2021; 1(3): 2021008.
2. Zheng J, Li Z, Shu X, et al. Tube spinning process: Recent advances and challenges. *J Adv Manuf Sci Tech* 2024; 4(4): 2024014.
3. Emmens WC, Sebastiani G, van den Boogaard A H. The technology of Incremental Sheet Forming—A brief review of the history. *J Mater Process Technol* 2010; 210(8): 981-997.
4. Duflou JR, Habraken A-M, Cao J, et al. Single point incremental forming: state-of-the-art and prospects. *Int J Mater Form* 2018; 11(6): 743-773.
5. Guzmán CF, Yuan S, Duchêne L, et al. Damage prediction in single point incremental forming using an extended Gurson model. *Int J Solids Struct* 2018; 151: 45-56.
6. Gupta P, Szekeres A, Jeswiet J. Design and development of an aerospace component with single-point incremental forming. *Int J Adv Manuf Tech* 2019; 103(9-12): 3683-3702.
7. Su C, Lv S, Wang R, et al. Effects of forming parameters on the forming limit of single-point incremental forming of sheet metal. *Int J Adv Manuf Tech* 2021; 113(1-2): 483-501.
8. Su C, Zhao Z, Lv Y, et al. Effect of process parameters on plastic formability and microstructures of magnesium alloy in single point incremental forming. *J Mater Eng Perform* 2019; 28(12): 7737-7755.
9. Yoganjaneyulu G, Sathiya Narayanan C, Narayaasamy R. Investigation on the fracture behavior of titanium grade 2 sheets by using the single point incremental forming process. *J Manuf Process* 2018; 35: 197-204.
10. Li Z, Lu S, Zhang T, et al. Numerical prediction of ductile fracture in multi-stage single point incremental forming based on phenomenological modified Mohr–Coulomb. *Measurement* 2020; 154.
11. Bailly DBM, Hirt G, Pofahl T, et al. Analysis into differences between the buckling in single-point and two-point incremental sheet forming of components for self-supporting sheet metal structures. *Key Eng Mater* 2014; 622: 367-374.
12. Wu R, Liu X, Li M, et al. Investigations on deformation mechanism of double-sided incremental sheet forming with synchronous thermomechanical steel-aluminum alloy bonding. *J Mater Process Technol* 2021; 294.
13. Ao D, Gao J, Chu X, et al. Formability and deformation mechanism of

Ti-6Al-4V sheet under electropulsing assisted incremental forming. *Int J Solids Struct* 2020; 202: 357-367.
14. Zhang H, Chu X, Bao W, et al. Microstructure evolution of AZ31B sheet deformed by electric hot temperature-controlled single point incremental forming. *Mater Sci Eng*: *A* 2021; 823.
15. Yang DY, Bambach M, Cao J, et al. Flexibility in metal forming. *CIRP Annals* 2018; 67(2): 743-765.
16. Cao TS. Numerical simulation of 3D ductile cracks formation using recent improved Lode-dependent plasticity and damage models combined with remeshing. *Int J Solids Struct* 2014; 51(13): 2370-2381.
17. Ghorbel O, Mars J, Koubaa S, et al. Coupled anisotropic plasticity-ductile damage: Modeling, experimental verification, and application to sheet metal forming simulation. *Int J Mech Sci* 2019; 150: 548-560.
18. Niu Y, Wang Y, Shi Y. Effect of micro-alloying of Ca and Gd on microstructure and mechanical properties of Mg-Zn-Al alloy. *J Adv Manuf Sci Tech* 2023; 3(2): 2023003.
19. Bonora N, Gentile D, Pirondi A, et al. Ductile damage evolution under triaxial state of stress: theory and experiments. *Int J Plast* 2005; 21(5): 981-1007.
20. Yu F, Hendry MT, Jar PYB, et al. A coupled stress-triaxiality-dependent damage viscoplasticity model on crack initiation and propagation in high-strength rail steel. *Theor Appl Fract Mec* 2020; 109.
21. Zhu Y, Engelhardt MD. A nonlocal triaxiality and shear dependent continuum damage model for finite strain elastoplasticity. *Eur J Mech A Solids* 2018; 71: 16-33.
22. Murakami S. Continuum damage mechanics: a continuum mechanics approach to the analysis of damage and fracture. *Springer Ebooks* 2012; 41.B4:4731-4755.
23. Saanouni K. *Damage mechanics in metal forming: Advanced modeling and numerical simulation*. 2012.
24. Lemaitre J, Desmorat R. *Engineering damage mechanics: ductile, creep, fatigue and brittle failures*. 2005.
25. Saanouni K, Chaboche J-L. Computational damage mechanics: Application to metal forming. *Comp Struct Intergrity* 2003; 3: 321-376.
26. Ai S, Long H. A review on material fracture mechanism in incremental sheet forming. *Int J Adv Manuf Tech* 2019; 104(1-4): 33-61.
27. Wu R, Hu Q, Li M, et al. Evaluation of the forming limit of incremental sheet forming based on ductile damage. *J Mater Process Technol* 2021; 287.
28. Lou Y, Huh H. Prediction of ductile fracture for advanced high strength steel with a new criterion: Experiments and simulation. *J Mater Process Technol* 2013; 213(8): 1284-1302.
29. Lou Y, Huh H, Lim S, et al. New ductile fracture criterion for prediction of fracture forming limit diagrams of sheet metals. *Int J Solids Struct* 2012; 49(25): 3605-3615.
30. Mohsen S, Behrooz A, Roza D. Advanced virtual manufacturing systems: A review. *J Adv Manuf Sci Tech* 2023; 3(3): 2023009.
31. Su C, Zhang M, Yang H, et al. Study on forming limit of single-point progressive forming of AZ31B magnesium alloy under isothermal local loading. *Int J Adv Manuf Tech* 2021; 118(1-2): 221-236.
32. Hou Y, Du K, Min J, et al. A generalized, computationally versatile plasticity model framework - Part I: Theory and verification focusing on tension–compression asymmetry. *Int J Plast* 2023; 171.
33. Bouchard PO, Bourgeon L, Fayolle S, et al. An enhanced Lemaitre model formulation for materials processing damage computation. *Int J Mater Form* 2010; 4(3): 299-315.
34. Gu B, He J, Li S, et al. Anisotropic fracture modeling of sheet metals: From in-plane to out-of-plane. *Int J Solids Struct* 2020; 182-183: 112-140.
35. Hansong JI, Qinghua S, Munish Kumar G, et al. Grain scale modelling and parameter calibration methods in crystal plasticity finite element researches: a short review. *J Adv Manuf Sci Tech* 2021; 1(2): 2021005.
36. Zhuang X, Meng Y, Zhao Z. Evaluation of prediction error resulting from using average state variables in the calibration of ductile fracture criterion. *Int J Damage Mech* 2017; 27(8): 1231-1251.
37. Besson J. Continuum models of ductile fracture: a review. *Int J Damage Mech* 2009; 19(1): 3-52.
38. Bao Y, Wierzbicki T. On fracture locus in the equivalent strain and stress triaxiality space. *Int J Mech Sci* 2004; 46(1): 81-98.
39. Bai Y, Wierzbicki T. A new model of metal plasticity and fracture with pressure and Lode dependence. *Int J Plast* 2008; 24(6): 1071-1096.
40. Gurson AL. Continuum theory of ductile rupture by void nucleation and growth: Part I—Yield criteria and flow rules for porous ductile media. *J Eng Mat Tech* 1977; 99(1): 2-15.
41. Needleman A, Tvergaard V. An analysis of ductile rupture in notched bars. *J Mech Phys Solids* 1984; 32(6): 461-490.
42. Tvergaard V. Influence of voids on shear band instabilities under plane strain conditions. *Int J Fracture* 1981; 17(4): 389-407.
43. Lemaitre J. A continuous damage mechanics model for ductile fracture. *Trans ASME J Eng Mate Tech*, 1985. 107(1): 83-89.
44. Kachanov LM. Time of the rupture process under creep conditions, Izy Akad. *Nank SSR Otd Tech Nauk* 1958; 8: 26-31.
45. Badreddine H, Labergère C, Saanouni K. Ductile damage prediction in sheet and bulk metal forming. *Comp Ren Méca* 2016; 344(4-5): 296-318.
46. Cao TS, Gachet JM, Montmitonnet P, et al. A Lode-dependent enhanced Lemaitre model for ductile fracture prediction at low stress triaxiality. *Eng Fract Mech* 2014; 124-125: 80-96.
47. Boudifa M, Saanouni K, Chaboche J-L. A micromechanical model for inelastic ductile damage prediction in polycrystalline metals for metal forming. *Int J Mech Sci* 2009; 51(6): 453-464.
48. Labergere C, Rassineux A, Saanouni K. Numerical simulation of continuous damage and fracture in metal-forming processes with 2D mesh adaptive methodology. *Finite Elem Anal Des* 2014; 82: 46-61.
49. Yue Z, Cao K, Badreddine H, et al. Failure prediction on steel sheet under different loading paths based on fully coupled ductile damage model. *Int J Mech Sci* 2019; 153-154: 1-9.
50. Mirnia MJ, Shamsari M. Numerical prediction of failure in single point incremental forming using a phenomenological ductile fracture criterion. *J Mater Process Technol* 2017; 244: 17-43.
51. Ambrogio G, Filice L, Manco GL. Warm incremental forming of magnesium alloy AZ31. *CIRP Annals* 2008; 57(1): 257-260.
52. Cui Z, Cedric XZ, Ren F, et al. Modeling and validation of deformation process for incremental sheet forming. *J Manuf Process* 2013; 15 (2): 236-241.
53. Kumar A, Gulati V, Kumar P, et al. Parametric effects on formability of AA2024-O aluminum alloy sheets in single point incremental forming. *J Mater Res Technol* 2019; 8(1): 1461-1469.
54. Pandre S, Morchhale A, Mahalle G, et al. Fracture limit analysis of DP590 steel using single point incremental forming: experimental approach, theoretical modeling and microstructural evolution. *Arch Civ and Mech Eng* 2021; 21(3).
55. Azaouzi M, Lebaal N. Tool path optimization for single point incremental sheet forming using response surface method. *Simul Model Pract Theory* 2012; 24: 49-58.
56. Dunand M, Mohr D. On the predictive capabilities of the shear modified Gurson and the modified Mohr–Coulomb fracture models over a wide range of stress triaxialities and Lode angles. *J Mech Phys Solids* 2011; 59(7): 1374-1394.
57. Beese AM, Luo M, Li Y, et al. Partially coupled anisotropic fracture model for aluminum sheets. *Eng Fract Mech* 2010; 77(7): 1128-1152.
58. Gorji M B, Mohr D. Predicting shear fracture of aluminum 6016-T4 during deep drawing: Combining Yld-2000 plasticity with Hosford–Coulomb fracture model. *Int J Mech Sci* 2018; 137: 105-120.
59. Li Y, Luo M, Gerlach J, et al. Prediction of shear-induced fracture in sheet metal forming. *J Mater Process Technol* 2010; 210(14): 1858-1869.
60. Roth CC, Mohr D. Ductile fracture experiments with locally proportional loading histories. *Int J Plast* 2016; 79: 328-354.
61. Mirnia MJ, Vahdani M, Shamsari M. Ductile damage and deformation mechanics in multistage single point incremental forming. *Int J Mech Sci* 2018; 136: 396-412.

62. Dizajyekan AZ, Mirnia MJ, Dariani BM. Fracture investigation in single point incremental forming of the Al/Cu laminated sheets using coupled damage plasticity model. *CIRP J Manuf Sci Tec* 2023; 43: 242-259.
63. Bharti S, Gupta A, Krishnaswamy H, et al. Evaluation of uncoupled ductile damage models for fracture prediction in incremental sheet metal forming. *CIRP J Manuf Sci Tec* 2022; 37: 499-517.
64. Zhan X, Wang Z, Li M, et al. Investigations on failure-to-fracture mechanism and prediction of forming limit for aluminum alloy incremental forming process. *J Mater Process Technol* 2020; 282.
65. Xue L, Wierzbicki T. Ductile fracture initiation and propagation modeling using damage plasticity theory. *Eng Fract Mech* 2008; 75(11): 3276-3293.
66. Malcher L, Andrade Pires FM, César de Sá JMA. An extended GTN model for ductile fracture under high and low stress triaxiality. *Int J Plast* 2014; 54: 193-228.
67. Gatea S, Ou H, Lu B, et al. Modelling of ductile fracture in single point incremental forming using a modified GTN model. *Eng Fract Mech* 2017; 186: 59-79.
68. Chang Z, Chen J. A new void coalescence mechanism during incremental sheet forming: Ductile fracture modeling and experimental validation. *J Mater Process Technol* 2021; 298.
69. Peng W, Ou H. Deformation mechanisms and fracture in tension under cyclic bending plus compression, single point and double-sided incremental sheet forming processes. *Int J Mach Tool Manu* 2023; 184: 103980.
70. Saanouni K. On the numerical prediction of the ductile fracture in metal forming. *Eng Fract Mech* 2008; 75(11): 3545-3559.
71. Badreddine H, Saanouni K, Dogui A. On non-associative anisotropic finite plasticity fully coupled with isotropic ductile damage for metal forming. *Int J Plast* 2010; 26(11): 1541-1575.
72. Zhang K, Badreddine H, Saanouni K. Ductile fracture prediction using enhanced CDM model with Lode angle-dependency for titanium alloy Ti-6Al-4V at room temperature. *J Mater Process Technol* 2020; 277: 116462.
73. Zhang K, Badreddine H, Hfaiedh N, et al. Enhanced CDM model accounting of stress triaxiality and Lode angle for ductile damage prediction in metal forming. *Int J Damage Mech* 2021; 30(2): 260-282.
74. Said L B, Mars J, Wali M, et al. Numerical prediction of the ductile damage in single point incremental forming process. *Int J Mech Sci* 2017; 131-132: 546-558.
75. Bouhamed A, Mars J, Jrad H, et al. Identification of fully coupled non-associated-Ductile damage constitutive equations for thin sheet metal applications: Numerical feasibility and experimental validation. *Thin-Walled Struct* 2022; 176: 109365.
76. Jin K, Guo X, Tao J, et al. A model of one-surface cyclic plasticity with Lemaitre damage criterion for plastic instability prediction in the incremental forming process. *Int J Mech Sci* 2016; 114: 88-97.
77. Yue Z, Chu X, Gao J. Numerical simulation of incremental sheet forming with considering yield surface distortion. *Int J Adv Manuf Tech* 2017; 92(5-8): 1761-1768.
78. Zhang K, Yue Z M, Su C J, et al. Modelling of ductile damage in single point incremental forming process using enhanced CDM model. *IOP Conference Series: Materials Science and Engineering* 2022; 1270(1).
79. Liu X, He J, Huang S. Mechanistically informed artificial neural network model for discovering anisotropic path-dependent plasticity of metals. *Mater. Design* 2023; 226.
80. Nagargoje A, Kankar PK, Jain PK, et al. Application of artificial intelligence techniques in incremental forming: a state-of-the-art review. *J Intell Manuf* 2021; 34(3): 985-1002.